The Astrophysical Journal, 890:71 (13pp), 2020 February 10 https://doi.org/10.3847/1538-4357/ab6a17

Broad-line Region of the Quasar PG 2130+099 from a Two-year Reverberation Mapping Campaign with High Cadence

Chen Hu[1], Yan-Rong Li[1], Pu Du[1], Zhi-Xiang Zhang[1,3], Sha-Sha Li[1,3], Ying-Ke Huang[1,3], Kai-Xing Lu[4], Jin-Ming Bai[4], Luis C. Ho[5,6], Wei-Hao Bian[7], Michael S. Brotherton[8], Ye-Fei Yuan[3], Jesús Aceituno[9,10], Hartmut Winkler[11], and Jian-Min Wang[1,2,12]
Seambh Collaboration

[1] Key Laboratory for Particle Astrophysics, Institute of High Energy Physics, The Chinese Academy of Sciences, 19B Yuquan Road, Beijing 100049, People's Republic of China; huc@ihep.ac.cn, wangjm@ihep.ac.cn
[2] School of Astronomy and Space Science, University of Chinese Academy of Sciences, 19A Yuquan Road, Beijing 100049, People's Republic of China
[3] Department of Astronomy, University of Science and Technology of China, Hefei 230026, People's Republic of China
[4] Yunnan Observatories, The Chinese Academy of Sciences, Kunming 650011, People's Republic of China
[5] Kavli Institute for Astronomy and Astrophysics, Peking University, Beijing 100871, People's Republic of China
[6] Department of Astronomy, School of Physics, Peking University, Beijing 100871, People's Republic of China
[7] Physics Department, Nanjing Normal University, Nanjing 210097, People's Republic of China
[8] Department of Physics and Astronomy, University of Wyoming, Laramie, WY 82071, USA
[9] Centro Astronomico Hispano Alemán, Sierra de los filabres sn, E-04550 Gergal, Almería, Spain
[10] Instituto de Astrofísica de Andalucía, Glorieta de la astronomía sn, E-18008 Granada, Spain
[11] Department of Physics, University of Johannesburg, P.O. Box 524, 2006 Auckland Park, South Africa
[12] National Astronomical Observatories of China, The Chinese Academy of Sciences, 20A Datun Road, Beijing 100020, People's Republic of China
Received 2018 July 11; revised 2019 December 31; accepted 2020 January 2; published 2020 February 13

Abstract

As one of the most interesting Seyfert 1 galaxies, PG 2130+099 has been the target of several reverberation mapping (RM) campaigns over the years. However, its measured broad Hβ line responses have been inconsistent, with time lags of ∼200 days, ∼25 days, and ∼10 days being reported for different epochs while its optical luminosity changed no more than 40%. To investigate this issue, we conducted a new RM-campaign with homogenous and high cadence (about ∼3 days) for two years during 2017–2019 to measure the kinematics and structure of the ionized gas. We successfully detected time lags of broad Hβ, He II, He I, and Fe II lines with respect to the varying 5100 Å continuum, revealing a stratified structure that is likely virialized with Keplerian kinematics in the first year of observations, but an inflow kinematics of the broad-line region from the second year. With a central black hole mass of $0.97^{+0.15}_{-0.18} \times 10^7 M_\odot$, PG 2130+099 has an accretion rate of $10^{2.1\pm0.5} L_{\rm Edd} c^{-2}$, where $L_{\rm Edd}$ is the Eddington luminosity and c is speed of light, implying that it is a super-Eddington accretor and likely possesses a slim, rather than thin, accretion disk. The fast changes of the ionization structures of the three broad lines remain puzzling.

Unified Astronomy Thesaurus concepts: Supermassive black holes (1663); Seyfert galaxies (1447); Active galactic nuclei (16); Quasars (1319); Reverberation mapping (2019); Time domain astronomy (2109)

Supporting material: machine-readable table

1. Introduction

Reverberations, the responses of broad emission lines to a changing continuum (Bachall et al. 1972; Blandford & McKee 1982), convey invaluable information about the kinematics and structure of the broad-line regions (BLRs) of Seyfert 1 galaxies (Peterson 2014, for a review). As an outlier of the well-known R–L relation discussed by Bentz et al. (2013), the Seyfert 1 galaxy PG 2130+099 ($m_V = 14.3$, $z = 0.063$) has drawn much attention in recent years. This intriguing object is a candidate super-Eddington accreting massive black hole (SEAMBH), as it shares the weak [O III] lines, strong Fe II emission, and Lorentzian broad Hβ profile with others of the class (Du et al. 2015). However, the reported Hβ time lags are mostly inconsistent with the characteristically short lags of SEAMBHs.

Kaspi et al. (2000) obtained a broad Hβ line time lag of $\tau_{\rm H\beta} = 188^{+136}_{-27}$ days from nearly eight-year monitoring between 1990 and 1998, but their campaign had very low cadence (the median sampling is $\gtrsim$20 days). In a 2007 campaign, Grier et al. (2008) measured a lag of $\tau_{\rm H\beta} = 22.9^{+4.4}_{-4.3}$ days, which is roughly an order of magnitude shorter. They claimed that the data of Kaspi et al. (2000) is generally too undersampled to measure a short lag, and that the $\tau_{\rm H\beta} = 188$ days could be caused by the secular long-term variability of the Hβ line. However, the time span of the Grier et al. (2008) data is also too short (only ∼100 days) to measure a long lag, and the cadence is not uniform, while the number of epochs is rather small as well (only 21).

Grier et al. (2012) monitored PG 2130+099 once again in 2010, with much better sampling of ∼1 days in median and a longer campaign duration of ∼120 days, but the Hβ lag again differed from previous investigations. They obtained $\tau_{\rm H\beta} = 12.8^{+1.2}_{-0.9}$ days from the likelihood method, and $\tau_{\rm H\beta} = 9.6 \pm 1.2$ days from the CCF methods with $r_{\rm max}$ only ∼0.35. Grier et al. (2013b) obtained a velocity-resolved delay for the 2010 campaign, but only four velocity bins were good enough for Hβ lags (see their Figure 7), and there are two peaks (∼10 and ∼30 days, and even a third at ∼50 days at the very edge) in the transfer function (see their Figure 15). Their two-dimensional transfer function shows the dominant response with ∼30 days from the maximum-entropy method (see their Figure 12). Grier et al. (2013b) note that their campaign missed

some potentially important epochs, and that this affected the accuracy of their results. The Hβ lags are complex although Bentz et al. (2013) prefers $\tau_{H\beta} \approx 30$ days. Grier et al. (2017) calculated a dynamical model for the Hβ-emitting region that is a thick Keplerian disk, but their model does not match the late one-third of the entire light curve (see their right panel of Figure 2), and seems to ignore the inflow component clearly visible in the results of Grier et al. (2013b).

Once again, this enigmatic object requires additional observations to determine its behavior, BLR structure and Hβ time lag. In this paper, we report results of a spectral monitoring campaign of PG 2130+099 mainly based on observations with the the Centro Astronómico Hispano-Alemán (CAHA) 2.2 m telescope at the Calar Alto Observatory in Spain. We successfully detected reverberations of several broad emission lines and thus have robust measurements of the BLR. Implications for our understanding of the BLR are discussed concerning the presence of multiple substructures. We use a cosmology with $H_0 = 70\,\mathrm{km\,s^{-1}\,Mpc^{-1}}$ and $\Omega_M = 0.3$.

2. Observations and Data Reduction

Since 2017 May, the SEAMBH project (Du et al. 2014) has expanded to make use of the CAHA 2.2m telescope to perform measurements focusing on PG quasars with high accretion rates (hereafter the CAHA-SEAMBH project). Given the uncertainties about its time lag and mass, PG 2130+099 is one of highest priorities of the CAHA-SEAMBH project. The monitoring was carried out at the telescope with the Calar Alto Faint Object Spectrograph (CAFOS) for 53 nights between 2017 June 22 (hereafter the year of 2017 observations) and 2018 January 4, and 58 nights between 2018 May 31 and 2019 January 16 (hereafter the year of 2018 observations). The strategy of observations is similar to that of the SEAMBH campaign performed at the Lijiang 2.4 m telescope of the Yunnan Observatories, Chinese Academy of Sciences (Du et al. 2014). For each night, broadband images of the object were obtained, then a long slit with a projected width of 3.″0 was carefully oriented and the spectra of the object and a nearby nonvarying comparison star were taken simultaneously. The typical displacement between the object and comparison star perpendicular to the slit direction was less than 0.5 pixel (0.″265), meaning that both are similarly affected by seeing losses, and thus enabling high-accurate flux calibration (the typical seeing was less than 2″). The position angle of the comparison star is 248°, and its angular separation from PG2130+099 is 86″. The Sloan Digital Sky Survey (SDSS; York et al. 2000) gives the magnitude of the comparison star in g band as 15.1. Our spectra show the comparison to be a G-type star. The typical S/N of the comparison star is ∼50 per pixel around 5200 Å, corresponding to the Hβ wavelength range of PG 2130+099 in the observed frame, which is sufficient for our requirement of flux calibration. We also restricted the airmass in most observations to be less than 1.2 to minimize the effect of atmospheric differential refraction.

2.1. Photometry

The photometric images were obtained by CAFOS in direct imaging mode with a Johnson V filter. Typically, three exposures of 20 s were taken each individual night. The images were reduced following standard IRAF procedures. The flux of the object and the comparison star were measured through a circular aperture with a radius of 2.″1, and differential magnitudes were obtained relative to 17 other stars within the field of 8.′8 × 8.′8.

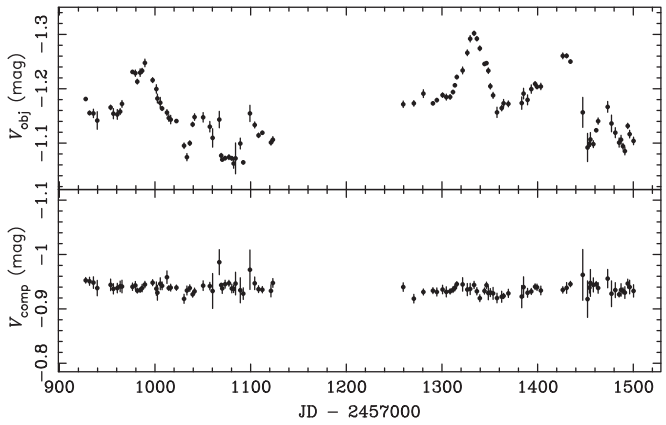

Figure 1. Light curves in the V band for PG 2130+099 (top) and the comparison star (bottom). The scatter in the magnitudes of the comparison star is ∼0.01 mag.

Figure 1 shows the light curves of the differential magnitudes for the object (top) and the comparison star (bottom), respectively. The accurate of the photometry is ∼0.01 mag, estimated from the scatter in the magnitudes of the comparison star. It also shows that this comparison star is stable enough to be used for the flux calibration of the spectroscopy.

2.2. Spectroscopy

The spectra of PG 2130+099 were taken using CAFOS with Grism G-200, which has a relatively high efficiency, without an order-blocking filter. The resulting spectra cover the observed-frame wavelength range of 4000–8500 Å, with a dispersion of 4.47 Å pixel^{-1}. Note that the second-order contamination occurs for wavelengths longer than ∼7000 Å, and has no effect on the measurements. A set of calibration frames was taken for each night, including bias frames, dome flats, and wavelength-calibration lamps of HgCd/He/Rb. For the object, two exposures of 600 s were taken during each individual night, and the typical signal-to-noise ratio (S/N) of the spectrum for a single exposure is ∼80 per pixel at rest frame 5100 Å. We took one or two spectrophotometric standards in the dusk and/or dawn of each night, if the weather and time allowed.

The spectra were reduced with IRAF following standard procedures: bias-removal, flat-fielding, wavelength calibration, and extraction to one-dimension. Extraction apertures were uniform and large (10.″6) to minimize light loss, especially on nights with poor seeing. The flux calibration of the object used the sensitivity function determined from the comparison star, as described below. First, for several nights with good weather conditions, the normal IRAF procedure of flux calibration was performed for the comparison star using spectrophotometric standards taken on the same night. Second, the calibrated spectra for those nights were combined to generate a fiducial spectrum of the comparison star. Then, for each exposure, a Legendre polynomial was fitted by comparing the extracted spectrum of the comparison star in counts to the fiducial spectrum. This Legendre polynomial serves as the sensitivity function and incorporates all corrections including the

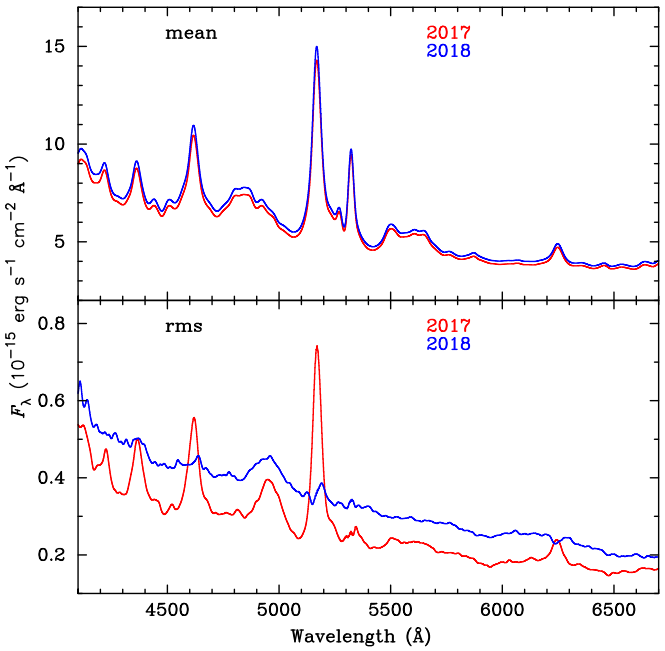

Figure 2. Mean (top) and rms (bottom) spectra for years 2017 (red) and 2018 (blue) separately. The mean spectra are almost the same, while the rms spectra are surprisingly different in the Balmer lines.

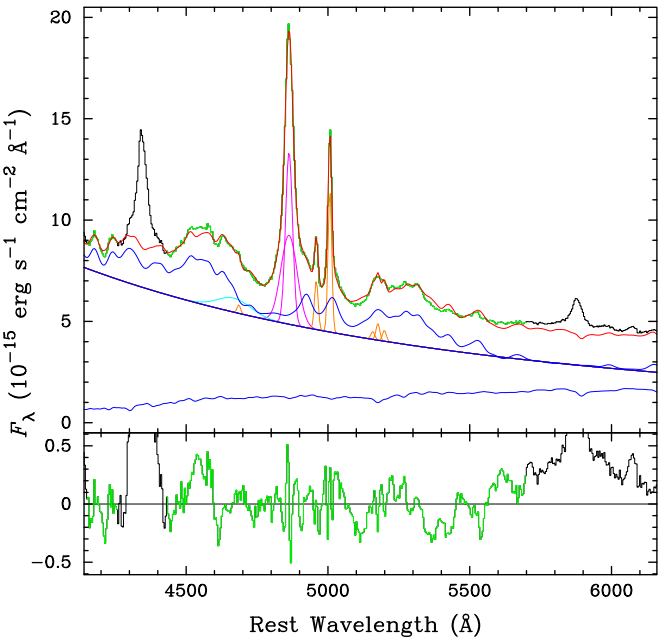

Figure 3. Spectral fitting scheme for an individual-night spectrum. The top panel shows the calibrated spectrum (green for fitted pixels and black for excluded) and the best-fit model (red), composed by the AGN power-law continuum (blue), Fe II emission (blue), host galaxy (blue), broad Hβ (magenta), broad He II (cyan), and narrow-emission lines (orange). The bottom panel shows the residuals. Details can be found in the main text.

atmosphere, slit loss, and instrumental sensitivity. Finally, the spectrum of the object for each exposure was flux-calibrated using the corresponding sensitivity function, and the two calibrated spectra for the same night were combined to obtain the individual-night spectrum for the following measurements and analysis.

The accuracy of the flux calibration using our comparison stars has been proven to be better than ∼3% (Du et al. 2018). In this specific case, it is better than 3% as estimated from the scatter of the [O III] light curve (see Section 3.1.2 for details). Figure 2 shows the mean (top) and rms (bottom) spectra for the years 2017 (red) and 2018 (blue) separately. The [O III] line almost vanishes in the rms spectrum, indicating that we have achieved good flux calibration. A prominent feature of the rms spectrum, compared to the mean spectrum, is the strong, broad He II emission line, indicating the strong variation in this line. The mean spectra for the two years are almost identical, and the variations of the Hβ profiles are also quite small compared with those in Kaspi et al. (2000) and Grier et al. (2012). However, the rms spectrum of 2018 is dramatically different in its almost vanishing Balmer lines.

2.3. Other Telescopes

In 2018, the object was also monitored by two other telescopes: the Lijiang 2.4 m telescope and the Sutherland 1.9 m telescope. Spectra were taken on three nights at the Lijiang 2.4 m telescope at the Yunnan Observatory of the Chinese Academy of Sciences, using the Yunnan Faint Object Spectrograph and Camera with grism G14 and a long slit of 2.″5. The slit was oriented to include the same comparison star as at CAHA, which is used for flux calibration. The spectra were extracted in an aperture of 2.″5 × 8.″5. The details of the spectroscopy and data reduction are given in Du et al. (2014). At the Sutherland station of the South African Astronomical Observatory, spectroscopic observations of PG 2130+099 were carried out with the 600 lines mm^{-1} grating and a slit of 0.″9, on 12 nights. The flux calibration was done by scaling the flux of the narrow [O III] emission lines to be the same as the mean value in the CAHA spectra. The set of the observations and data reduction are the same as that described in Winkler & Paul (2017).

The epochs of the Lijiang spectra are rather few (only three nights), while the Sutherland spectra are calibrated by another method and the data quality is relatively scattered especially for the last four data points where technical problems caused a shift in the grating angle. So for the consistency of the data set, we used the data from CAHA only for the analysis below, but show the integrated light curves of the continuum and Hβ from Lijiang (green points) and Sutherland (blue points) in panels (a) and (c) of Figure 4.

3. Analysis Methods

3.1. Light-curve Measurements

There are several methods to measure the light curves. The traditional method adopted in most RM studies (e.g., Kaspi et al. 2000; Peterson et al. 2004; Du et al. 2018) employs integration over a range of relevant wavelengths, which is simple and usually robust for single, strong emission lines such as Hβ. But for those highly blended emission lines, e.g., Fe II emission which forms a pseudo-continuum, a spectral-fitting scheme (SFS) has proven to be necessary to measure the light curves (Bian et al. 2010; Barth et al. 2013; Hu et al. 2015). In some cases, especially for nearby Seyferts, spectral fitting can improve the measurements for even the Hβ emission line, by modeling and removing the contamination of strong host galaxy contribution which varies from night to night due to seeing and guiding variations (Hu et al. 2015, 2016). However, comparing with integration, the spectral fitting scheme requires

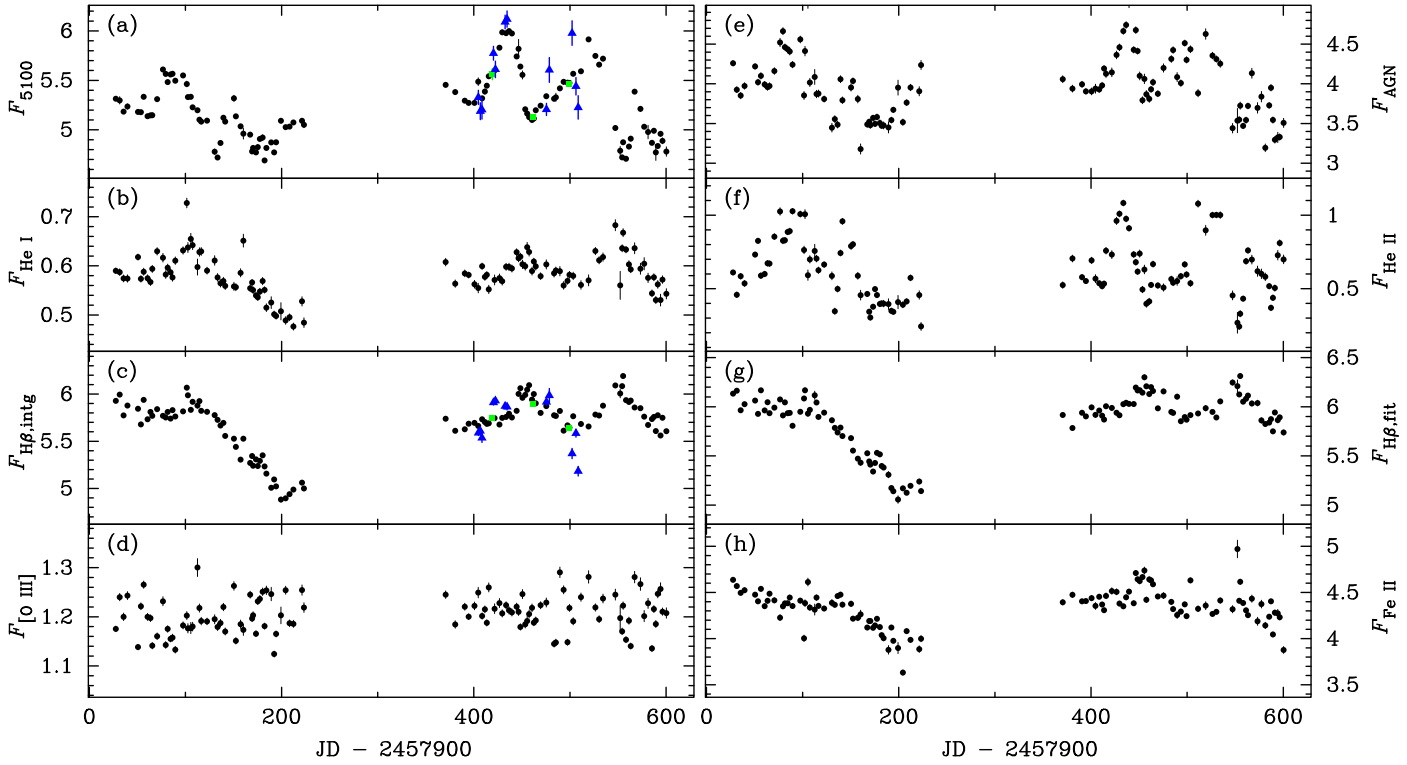

Figure 4. Light curves of continuum and emission lines. Panels (a)–(c) show those measured by the integration scheme, whereas (d)–(h) by the spectral fitting scheme. The green and blue data points in panels (a) and (c) are observed by the Lijiang 2.4 m telescope and the Sutherland 1.9m telescope, respectively. The units of the continuum fluxes in panels (a) and (e) are $\times 10^{-15}$ erg s^{-1} cm^{-2} Å^{-1}, and the units of the emission line fluxes in other panels are $\times 10^{-13}$ erg s^{-1} cm^{-2}. See details in the main text.

higher quality of the data. For example, for reliable decomposition of the host starlight, the wavelength coverage of the spectrum should be wide, and the shape of the spectrum has to be especially well calibrated. These requirements can be difficult to achieve with the [O III]-calibration mode of RM campaigns since only a constant scaling factor is applied for the whole wavelength range. Sometimes, integration and fitting are combined to use the advantages of both methods: subtracting the continuum by spectral fitting and then integrating the residual flux to measure the light curves of emission lines (Barth et al. 2013, 2015).

For fitting the spectra of PG 2130+099 here, besides an AGN power law, a host starlight template is needed to model the continuum shape accurately. However, the host starlight contribution is rather weak in this luminous PG object, and also the spectral resolution is low; our spectra do not show prominent absorption features of host starlight. Thus, the host starlight component cannot be modeled well and its apparent variation due to seeing and mis-centering cannot be removed by spectral fitting as precisely as for other sources (Hu et al. 2015, 2016). In fact, the uncertainty in fitting the host starlight could introduce extra systematic errors into the light-curve measurements. So in this work, we used both methods in this manner: integration for the measurements of the AGN continuum, Hβ, and He I, and the fitting method for the highly blended Fe II and He II features.

3.1.1. Integration Scheme

Taking the following windows of Hβ: 4810–4910Å and He I: 5950–6000 Å in the rest frame, respectively, we integrate across them for the Hβ and He I lines. For each emission line, a straight line was defined by the two continuum windows located on the sides of the emission, and then the flux above this straight line was integrated in the emission line window. The average flux in the redward continuum window of Hβ, 5085–5115 Å, was calculated as the integrated 5100 Å flux (F_{5100}). Note that the individual-night spectra were corrected for the Galactic extinction and de-redshifted before the integration, to enable the comparison of the light curves given by integration and fitting. We assumed an extinction law with $R_V = 3.1$ (Cardelli et al. 1989; O'Donnell 1994) and adopted a V-band extinction of 0.122 mag obtained from the NASA/IPAC Extragalactic Database of Schlafly & Finkbeiner (2011). Light curves are given in Figure 4, panels (a)–(c).

3.1.2. Spectral Fitting Scheme

The SFS follows Hu et al. (2015) with some changes described below to suit the difficulty of decomposing the host starlight in our spectra. Figure 3 shows an example of the fit to an individual-night spectrum. The following components are included in our fitting: (1) a single power law for the AGN continuum, (2) Fe II emission modeled by convolving the template from (Boroson & Green 1992) with a Gaussian function, (3) the host galaxy starlight modeled by the template with 11 Gyr age and metallicity $Z = 0.05$ from Bruzual & Charlot (2003), (4) a double Gaussian for Hβ, (5) a single Gaussian for He II, (6) a set of several single Gaussians with the same velocity width and shift for narrow-emission lines including [O III] $\lambda\lambda$4959, 5007, He II λ4686, and several coronal lines. The narrow Hβ line is not included in the fitting because of its weakness ($\sim$2% of the total Hβ flux estimated using [O III] line, see Section 4.1 for details) and the low

Table 1
Light Curves of 5100 Å Continuum and Several Lines

JD-2457,900	F_{5100}	$F_{H\beta}$	$F_{He\ I}$	$F_{He\ II}$	F_{Fe}
27.637	5.314 ± 0.017	5.927 ± 0.010	0.590 ± 0.006	0.610 ± 0.015	4.636 ± 0.020
31.593	5.298 ± 0.037	5.993 ± 0.012	0.587 ± 0.007	0.459 ± 0.018	4.569 ± 0.025

Note. The 5100 Å continuum flux is in units of 10^{-15} erg s^{-1} cm^{-2} Å^{-1}, and all lines are in units of 10^{-13} erg s^{-1} cm^{-2}.
(This table is available in its entirety in machine-readable form.)

Table 2
Reverberations of Several Broad Lines from the Present Campaign

Line	F_{var} (%)		Lag (days)		FWHM (km s^{-1})		Virial Product ($\times 10^7 M_\odot$)		CCF Broadening (days)	
	2017	2018	2017	2018	2017	2018	2017	2018	2017	2018
He II	32.7 ± 3.6	29.9 ± 3.0	$-1.4^{+6.8}_{-0.9}$	$-2.9^{+1.5}_{-0.9}$	6049 ± 187	9589 ± 774	...	...	5	−7
He I	8.2 ± 0.9	4.2 ± 0.6	$18.2^{+7.3}_{-3.1}$	$31.1^{+2.9}_{-5.8}$	2547 ± 18	2497 ± 14	$2.30^{+0.93}_{-0.39}$	$3.78^{+0.35}_{-0.70}$	17	7
Hβ	6.1 ± 0.6	2.3 ± 0.3	$22.6^{+2.7}_{-3.6}$	$27.8^{+2.9}_{-2.9}$	2101 ± 100	2072 ± 107	$1.95^{+0.30}_{-0.36}$	$2.33^{+0.34}_{-0.34}$	31	12
Fe II	4.8 ± 0.5	3.3 ± 0.5	$35.3^{+8.2}_{-9.9}$	$23.1^{+3.4}_{-5.6}$	2047 ± 94	1944 ± 95	$2.88^{+0.72}_{-0.85}$	$1.70^{+0.30}_{-0.45}$	48	16

Note. The virial product is defined by Equation (1). See the text for details of the measurements of FWHM for each line. It should be pointed out that F_{var} has different meanings from the calibration uncertainties.

spectral resolution prevent a reliable decomposition of it in individual-night spectra. Thus, the narrow Hβ line is ignored and the double Gaussian of component (4) above are used for the measurements of broad Hβ. The He II lines are weak and blended with Fe II emission in individual-night spectra and even the mean spectrum, but prominent in the rms spectrum. Thus the velocity width and shift of He II are fixed to the values given by the best fit to the rms spectrum. Also, the coronal lines are weak and blended with Fe II emission, thus the flux ratios of the narrow-emission lines relative to [O III] λ5007 are fixed to the values given by the best fit to the mean spectrum, as in Hu et al. (2015). The only difference between the fitting here and that in Hu et al. (2015) is the treatment of the host galaxy. The spectra of PG 2130+099 do not show prominent absorption features because of the weakness of its host galaxy and also the low spectral resolution (with an instrumental broadening of ∼ 1000 km s^{-1} in FWHM). So the velocity width and shift of the host galaxy are fixed to those of [O III] λ5007 in the best fit to the mean spectrum. The flux of the host starlight is allowed to vary, but the slope of the AGN continuum is fixed to the best-fit value of the mean spectrum, as in Hu et al. (2015). In total, there are 15 free parameters, the other 17 are fixed.

The fitting is performed in the wavelength range 4150–5700 Å, excluding a narrow window around Hγ. We try to extend the fit redward to include the He I λ5876 emission line. However, as shown as the residual in Figure 3, this emission line seems to have a very broad wing, or the continuum around it is not well modeled due to the uncertain host galaxy component. Including this wavelength range in the fitting makes the resulting continuum light curve more uncertain, that the systematic error (estimated by the scatter in the fluxes of successive nights) becomes larger. Also, the light curve of the fitted He I resembles that from the integration method, but with slightly larger scatter. So we do not include He I λ5876 in the fitting, and adopt its light curve from direct integration.

Figure 4 panels (d)–(h) show the light curves generated from the best-fit values of the corresponding parameters: [O III] flux, the flux density of the power law at 5100 Å (F_{AGN}), He II flux ($F_{He\ II}$), Hβ flux ($F_{H\beta,fit}$), and Fe II flux (F_{Fe}). The flux of [O III] ideally should be a constant (Peterson et al. 2013), thus the scatter of the measured [O III] flux can be used to estimate the accuracy of the flux calibration. In this case, [O III] is relatively weak and its measurement has extra uncertainty resulting from the blending of the Fe II emission. So the scatter of 3%, which should be considered to be an upper limit of the flux calibration accuracy, is comparable with other RM campaigns (e.g., Peterson et al. 1998a; Kaspi et al. 2000; Barth et al. 2015; Fausnaugh 2017).

The F_{AGN} light curve resembles that of F_{5100}, but with larger scatter. This is caused by the uncertainty in the host galaxy component mentioned above. The Hβ light curves given by the fitting and simple integration are almost the same, which is expected for a strong, single emission line (Hu et al. 2015). The fluxes obtained by fitting are larger than those by integration, because of inclusion of the flux of the broad wings which are outside of the window of integration.

4. Results

4.1. Lags of the Broad Emission Lines

We use the light curves of the continuum at 5100 Å, Hβ, and He I from integration, and He II and Fe II from spectral fitting, for the following time-series analysis. Table 1 lists all these light curves. The errors of the fluxes listed in this table are those generated from the errors of each pixel in the observed spectra, and are usually not large enough to interpret the scatter in the fluxes of successive nights. So an additional systematic error was calculated for each light curve using the same method as in Du et al. (2014), and all the analysis below was done taking account of this systematic error. We first calculate the variability amplitude F_{var}, defined by Rodríguez-Pascual et al. (1997), for

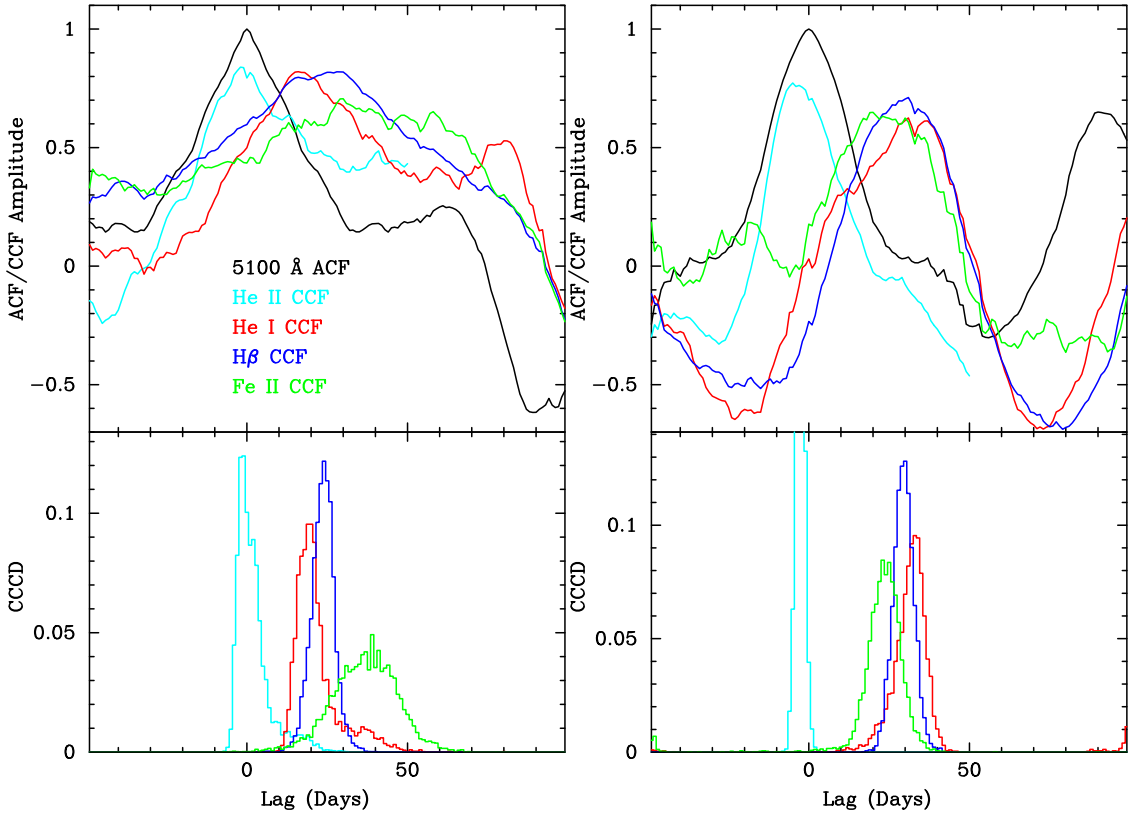

Figure 5. Cross-correlation analyses of Hβ, He I, He II, and Fe II lines with 5100 Å continuum, for 2017 (left) and 2018 (right), respectively.

each light curve. The quantity represents the intrinsic variability over the errors in the measurements (including the additional systematic error). Its uncertainties are calculated as defined by Edelson et al. (2002). Table 2 lists the results. As mentioned in Section 3.1.2 above, the weak narrow Hβ component has not been subtracted from our measurements of broad Hβ. The flux of [O III] λ5007 line is $1.21 \pm 0.04 \times 10^{-13}$ erg s^{-1} cm^{-2}, measured from the light curve of [O III] in panel (d) of Figure 4. Assuming a typical value of 0.1 for the narrow Hβ/[O III] intensity ratio in AGNs (e.g., Veilleux & Osterbrock 1987), the narrow Hβ component contributes only $\sim$2% fluxes of the Hβ measured here. Thus, the dilution of Hβ $F_{\rm var}$ by the uncorrected narrow component is negligible. Note that He II has an $F_{\rm var}$ much larger than the other emission lines, and even the continuum. This behavior is also shown by the strong He II emission feature in the rms spectrum (see the bottom panel of Figure 2), and common for many objects in previous RM investigations (Barth et al. 2015).

We measured the reverberation lags between the variations of the continuum (F_{5100}) and emission lines ($F_{\rm He\,II}$, $F_{\rm He\,I,intg}$, $F_{\rm H\beta,intg}$, and $F_{\rm Fe}$), using the standard interpolation cross-correlation function (CCF) method (Gaskell & Sparke 1986; Gaskell & Peterson 1987; White & Peterson 1994). The centroid of the CCF, using only the part above 80% of its peak value ($r_{\rm max}$), is adopted as the time lag (Koratkar & Gaskell 1991; Peterson et al. 2004). The error of the time lag is given by the 15.87% and 84.13% quantiles of the cross-correlation centroid distribution (CCCD) generated by 5000 Monte Carlo realizations, following Maoz & Netzer (1989) and Peterson et al. (1998b). In each realization, a subset of data points is selected randomly, and their fluxes are also changed by random Gaussian deviations according to the errors. The top panel of Figure 5 shows the autocorrelation function (ACF) of the F_{5100} light curve (in black), and also the CCFs for the emission lines (He II in cyan, He I in red, Hβ in green, and Fe II in blue) with respect to F_{5100}. The bottom panel shows the corresponding CCCDs for the CCFs. The measured time lags are listed in Table 2.

4.2. Line Profile Measurements

For Hβ and Fe II, which are included in the fitting and allowed to vary, the means of their velocity widths and shifts obtained from the best fits to individual-night spectra are adopted to be the measurements of their line profiles. The standard deviations are used as the errors. For He II, the velocity width and shift are measured from the rms spectrum. For He I, we perform an additional fit to a narrow band of the spectrum around the emission line including only a straight line as the continuum and a single Gaussian for He I. Their errors are estimated by Monte Carlo simulation: several realizations of mean and rms spectra were generated by bootstrap sample selection, and the same spectral fitting was performed and the velocity widths were measured. Then the standard deviations of the velocity widths measured from the realizations are used as the errors.

The resolution is estimated by comparing the width of [O III] in our spectra (FWHM = 1084 km s^{-1}) to those from previous high-spectral-resolution observations. Whittle (1992) obtained an [O III] FWHM measurement of 350 km s^{-1} (see also Grier et al. 2012), yielding a broadening of 1020 km s^{-1}. We also fit the spectrum of this object from Boroson & Green (1992), obtained an [O III] FWHM of 400 km s^{-1} after correcting for

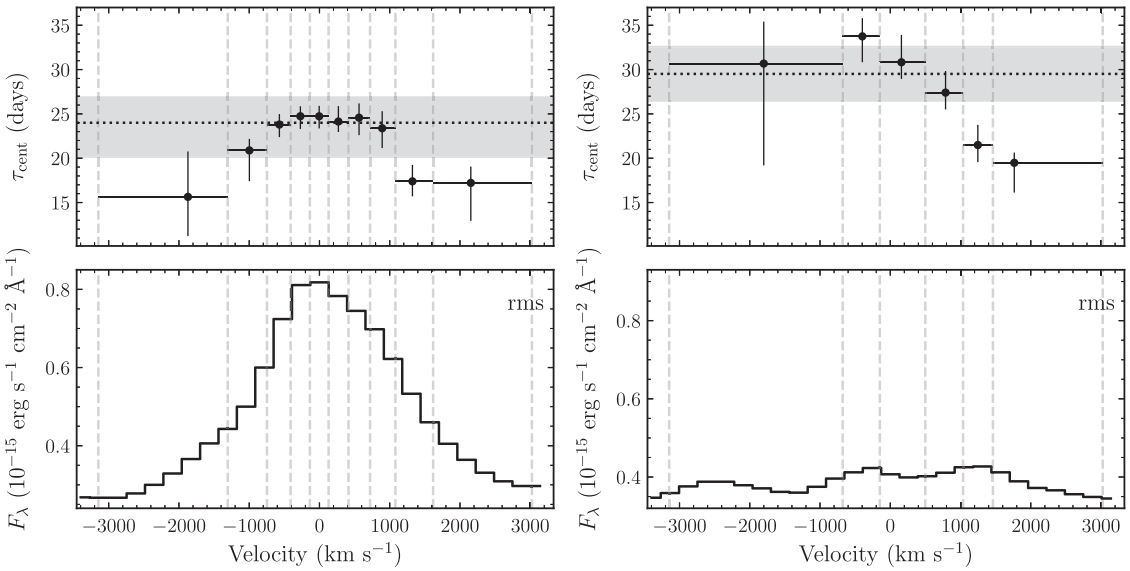

Figure 6. Velocity-resolved delays from 2017 (left) and 2018 (right) observations, showing very different shapes. Observations in 2017 show shorter time delays for high-velocity gas, consistent with the model of the Hβ-emitting region being in a virialized motion. In contrast, observations in 2018 show shorter lags in the red wing, which is more likely generated from an infall. Light curves and CCF analysis are given for each velocity bin in Appendix A.

Table 3
Hβ Line Width Information

	Mean Spectra		Rms			
	$\sigma_{\rm line}$		FWHM		$\sigma_{\rm line}$	
Year	2017	2018	2017	2018	2017	2018
Width	1437 ± 64	1438 ± 41	2447 ± 73	2054 ± 557	1272 ± 97	874 ± 237
$\hat{M}$.($10^7 M_\odot$)	$0.91^{+0.14}_{-0.17}$	$1.12^{+0.13}_{-0.13}$	$2.64^{+0.35}_{-0.45}$	$2.29^{+1.26}_{-1.26}$	$0.71^{+0.14}_{-0.16}$	$0.41^{+0.23}_{-0.23}$

Note. The width is in units of km s^{-1} and after instrumental broadening correction. Here the values were measured from the rms spectra shown in Figure 2, without the deconvolution in Section 4.3. The blue peak around -2500 km s^{-1} in the rms spectrum after deconvolution in Figure 6 is not high enough to contribute the FWHM listed here.

their instrument broadening. The resultant broadening is similar, and we adopted an FWHM $= 1000$ km s^{-1} as the instrument broadening of our spectra. The measurements of the widths of each emission line after instrument broadening correction are listed in Tables 2 and 3.

4.3. Velocity-resolved Delays

In order to investigate the geometry and kinematics of the BLR in PG 2130+099, we calculated the velocity-resolved time lags of the Hβ emission line profile. First, the influence of the varying line-broadening functions (ψ) and wavelength-calibration inaccuracy for different nights, which are caused by the changing seeing and misalignment of the slit, must be removed. Using comparison stars, the line-broadening function can be obtained by fitting the spectra of the stars using a stellar template convolved by ψ. The wavelength-calibration inaccuracy is also taken into account as the velocity shift of ψ. We adopted the Richardson–Lucy deconvolution algorithm, which is demonstrated to be an efficient way to recover the signal blurred by a known response kernel, to correct the ψ function. Details of these mathematical manipulations are described by Du et al. (2016a). After the correction, the emission line is divided into several bins, each of which has the same flux in the rms spectrum. Then, the light curves in the bins and their corresponding time lags relative to the continuum light curve are measured as previously described.

Figure 6 shows the velocity-resolved time delays and the rms spectrum (after the line-broadening correction) obtained for 2017 (left) and 2018 (right), respectively. The figure indicates that the BLR in 2017 has a geometry of virialized motion (e.g., see plots in Welsh & Horne 1991; Bentz et al. 2009), while in 2018 it more likely has an infall structure. However, it should be pointed out that the bluest point in the right panel of Figure 6 has quite large error bars because of the weak response in the second year. Whether or not the BLR kinematics are consistent with inflow remains open, but it is certain that the variable BLR has changed between the two years. For the upcoming discussion, we refer to the BLR as an inflow in the second year. The exact description of the geometry should be given by the application of the maximum-entropy method (MEM) developed by Horne et al. (2004), which is out of the scope of this paper.

We note that the lags in both wings could be contaminated by the continuum subtraction. In order to test the contamination, we show the velocity-resolved delays with equal fluxes in the mean spectra in Appendix A. Light curves of each velocity

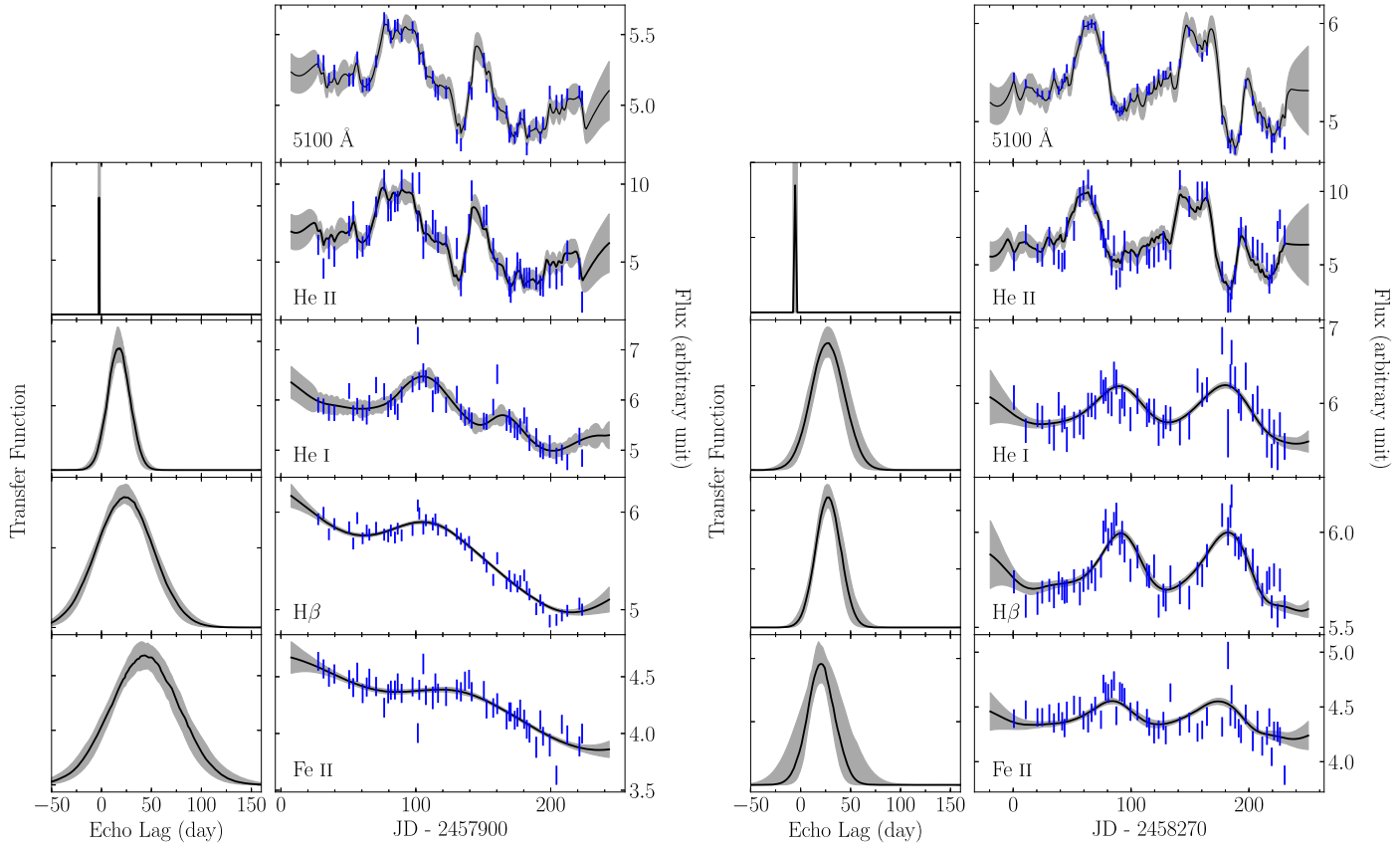

Figure 7. Transfer functions of the Hβ, He I, and Fe II lines from the first (left) and the second years (right).

Table 4
BLR Lags and Broadening from the Transfer Functions

Campaign	Hβ			He I			Fe II		
	τ	$\Delta\tau$	$\tau/\Delta\tau$	τ	$\Delta\tau$	$\tau/\Delta\tau$	τ	$\Delta\tau$	$\tau/\Delta\tau$
2017	23.2 ± 2.3	28.3 ± 3.2	0.8 ± 0.1	17.1 ± 1.6	11.0 ± 1.8	1.6 ± 0.2	43.3 ± 4.9	34.9 ± 4.2	1.3 ± 0.2
2018	27.6 ± 1.9	12.5 ± 2.6	2.2 ± 0.3	27.3 ± 2.1	16.9 ± 3.1	1.6 ± 0.3	20.5 ± 2.1	14.1 ± 7.1	1.4 ± 0.6

Note. (τ, $\Delta\tau$) are in units of days.

bin are shown in Appendix B as well as CCF analysis. Comparing them, we conclude that the influence is quite weak.

The data quality of other emission lines is not good enough to determine the velocity-resolved time lags.

4.4. Transfer Functions

Following the procedure in Li et al. (2016),[13] we used a Gaussian to parameterize the transfer function of each emission line. The amplitude, width, and central values of the Gaussian are free parameters and determined by a Markov Chain Monte Carlo (MCMC) method. The continuum variations are described by a damped random walk model. As such, the covariance functions between continuum and emission lines and between lines can be expressed analytically. This allowed us to employ the well-established framework given by Rybicki & Press (1992) to calculate the Bayesian posterior probabilities and infer the best values for free parameters.

[13] The procedure is implemented in the package MICA, which is publicly available at https://github.com/LiyrAstroph/MICA2.

Fitting results for the two years are shown by Figure 7 and listed in Table 4, separately. Lags obtained by the transfer functions are consistent with those of the CCF method.

4.5. Black Hole Mass and Accretion Rates

The bulge velocity dispersion of PG 2130+099 is $\sigma_* = 163 \pm 19\,\mathrm{km\,s^{-1}}$ from near-infrared spectra (Grier et al. 2013a), but the host galaxy has a pseudo-bulge ($n \approx 0.45$) and a disturbed disk (Kim et al. 2017). Using the same slope of the $M_\bullet$–σ_* relation (Kormendy & Ho 2013) but half of its zero-point (Ho & Kim 2015), we expect $M_\bullet \approx 6.5 \times 10^7 M_\odot$ in PG 2130+099. This estimate should be regarded as an upper limit. Indeed, Grier et al. (2017) made use of an MCMC method to model the BLR and to determine the black hole mass through Hβ light curves, and found $\log_{10}(M_\bullet/M_\odot) = 6.87^{+0.24}_{-0.23}$, which is significantly lower than that from the $M_\bullet$–σ relation. Comparing our velocity-resolved time lags in 2017 as shown by Figure 6 with the MCMC model (Grier et al. 2017), we find the model matches our measurements, leading to support of $M_\bullet = 10^{6.87} M_\odot$ as a conservative mass estimation.

Using the presently detected Hβ lags, we determine the virial product

$$\hat{M}_\bullet = \frac{c\tau_{\rm H\beta} \times V^2}{G}, \quad (1)$$

where G is the gravitational constant, V is either full width at half maximum ($V_{\rm FWHM}$) or velocity dispersion ($\sigma_{\rm line}$) of the Hβ profile in the mean spectrum or rms. We list $\hat{M}_\bullet$ in Tables 2 and 3, yielding the black hole mass if given the virial factor ($f_{\rm BLR}$). The $f_{\rm BLR}$ can in principle be calibrated by the $M_\bullet$–σ_* relation (e.g., Onken et al. 2004; Woo et al. 2015; Batiste et al. 2017), or the black hole masses from accretion disk models (Lü 2008; Mejía-Restrepo et al. 2017), but it tends to be smaller for AGNs with pseudo-bulges, such as $f_{\rm BLR} = 0.5$ (Ho & Kim 2014). If we take $f_{\rm BLR} = 0.5$, we have $M_\bullet = 0.97^{+0.15}_{-0.18} \times 10^7\, M_\odot$ from the virial product by using the mean FWHM of Hβ in 2017 (the BLR may significantly deviate from virialized state in the second year), agreeing with the MCMC result of black hole mass in Grier et al. (2017).

In light of the standard model of accretion disks (Shakura & Sunyaev 1973), the dimensionless accretion rates defined by $\dot{\mathscr{M}} = \dot{M}_\bullet / L_{\rm Edd} c^{-2}$ can be estimated as (Du et al. 2016b)

$$\dot{\mathscr{M}} = 20.1 \left(\frac{\ell_{44}}{\cos i}\right)^{3/2} M_7^{-2}, \quad (2)$$

if given the optical luminosity and the black hole mass, where $\dot{M}_\bullet$ is the accretion rate, and $L_{\rm Edd}$ is the Eddington luminosity, $\ell_{44} = L_{5100}/10^{44}$ erg s^{-1}, $M_7 = M_\bullet/10^7 M_\odot$, and i is the inclination of the disks (we take $\cos i = 0.75$[14]). The mean flux at 5100 Å in the first year is $\bar{F}_{5100} = (5.12 \pm 0.25) \times 10^{-15}$ erg s^{-1} cm^{-2} Å^{-1} corresponding to a mean luminosity $\lambda L_\lambda = (2.50 \pm 0.12) \times 10^{44}$ erg s^{-1} in the present epoch. With $M_\bullet$ and $\ell_{44} = 2.50$, we obtain $\dot{\mathscr{M}} = 10^{2.1\pm0.5}$, implying a super-Eddington accretor.

5. Discussions: Unresolved Questions

Results from the two years are shown in the previous section, but several puzzles arise. From Table 2, we find $R^{\rm 1st}_{\rm H\beta} = 22.6^{+2.7}_{-3.6}$ ltd and $R^{\rm 2nd}_{\rm H\beta} = 27.8^{+2.9}_{-2.9}$ ltd, showing that the Hβ region slightly changed in the two years (but the difference is less than two times the uncertainty, so could be caused by just uncertainties in the measurements). However, the radii of the He I and Fe II regions changed by a factor of almost 2.

It is useful to illustrate the dynamical timescale of the BLR variations defined as

$$\Delta t_{\rm BLR} = \frac{R_{\rm H\beta}}{V_{\rm H\beta}} = 8.2\, R_{20} V_{2000}^{-1}\ {\rm yr}, \quad (3)$$

where $R_{20} = R_{\rm H\beta}/20$ ltd is the BLR size in units of 20 ltd and $V_{2000} = V_{\rm H\beta}/2000$ km s^{-1} is the FWHM(Hβ) in units of 2000 km s^{-1}. It implies that the structure and kinematics of the BLR in PG 2130+099 cannot be significantly changed in two successive years but either the ionization structure could follow the variations of the ionizing source in one year, or some physical processes drive internal changes (i.e., some local variations in the BLR).

Note that the time lag of He II we measured is negative, but consistent with zero considering its uncertainty. Similar results have been reported for other objects (e.g., Barth et al. 2013). Keeping in mind the result that He II has a much larger variability amplitude than F_{5100}, a possible explanation of the negative/zero time lag is that He II is responding to the UV ionizing flux, which leads the optical continuum, as suggested by, e.g., Barth et al. (2013) and Edelson et al. (2019).

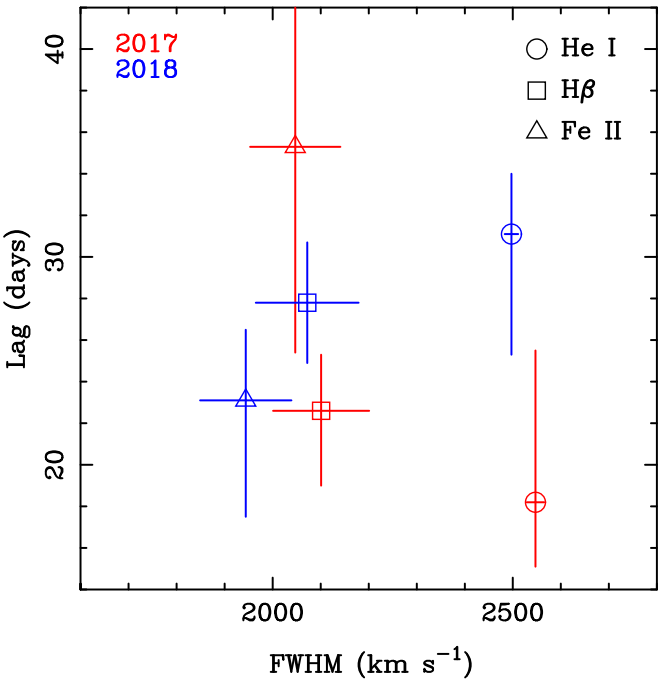

Figure 8. Time lag vs. FWHM of emission lines. The BLR does not conform to the onion structure in 2018.

5.1. Onion Structure

The onion structure of the BLR is quite well understood as a sequence of ionization energy of ions (Collin-Souffrin & Lasota 1988) and FWHM of lines (Peterson & Wandel 1999). The ions relevant to this study have ionization energies of $\epsilon_{\rm He\,II} = 54.4$ eV, $\epsilon_{\rm He\,I} = 24.58$ eV, $\epsilon_{\rm H\beta} = 13.6$ eV and $\epsilon_{\rm Fe\,II} = 7.87$ eV. From the first year, we have $R_{\rm Fe\,II} > R_{\rm H\beta} > R_{\rm He\,I} > R_{\rm He\,II}$, following the onion structure as shown by Figure 8.

In the observations of the second year, the Hβ-emitting region do not show significant variations; however, He I and Fe II regions show significant changes, in particular, $R_{\rm Fe\,II} \lesssim R_{\rm H\beta} \lesssim R_{\rm He\,I}$ disrupting the onion structure with a timescale much less than the dynamical time as shown by Equation (3). The first unresolved question would be to explain the mechanism that generates such a change in the onion structure.

5.2. Kinematics

The velocity-resolved delays of the broad Hβ line in the two years shown in Figure 6 are different. The responding emission line region shows a change from a virialized motion to an inflow on a timescale of less than one year. The profile and the intensity of the Hβ line in the rms spectra dramatically change.

[14] Grier et al. (2017) gives a value of $30.2^{+11.0}_{-10.1}$° for the inclination angle of this object from dynamically modeling, which is marginally consistent with our choice here. We still take cos $i = 0.75$ for a convenient comparison with other objects without inclination angle measurements.

It is a smooth core-dominated profile in the first year, but multiple-peaked and wing-dominated in the second. On the other hand, the widths of the broad lines in the mean spectrum remain almost the same as in the first year, as well as the virial products derived. This implies that the BLR may still be actually virialized in the second year. Such an inconsistency is worth further investigation: is the velocity-resolved delays in the second year a unique signature of infall as in those simple models? If so, why do the majority of Hβ-emitting clouds have virialized motions in the second year as shown by the mean spectrum, while the reverberation part has a kinematics of inflow indicated by the velocity-resolved delays? Furthermore, what is the connection between the inflow and the virialized part of the BLR? This is the second puzzle, which motivates us to continue monitoring PG2130+099.

5.3. Weak Reverberation

The variability amplitude of 5100 Å flux ($F_{\rm var} = 6.7\%$) in the second year is larger than that in the first year ($F_{\rm var} = 4.7\%$); however, Hβ is less variable in the second year ($F_{\rm var} = 2.3\%$) than in the first year ($F_{\rm var} = 6.1\%$). This means a weaker response of Hβ to the varying continuum in the second year. That the virialized part of the BLR did not respond in the second year may be consistent with the weak response, but it is hard to understand why. The transfer functions are also very different in the two years. Though the mean radius of Hβ-emitting region does not change much, the width ($\tau/\Delta\ \tau$) changes by a factor of 2 (see Table 4 and Figure 7). On the contrary, He I and Fe II mean radii change significantly, but their relative widths ($\tau/\Delta\tau$) stay almost unchanged. This is the third puzzle.

Photoionization calculations and light-curve simulations have been performed in the literature (e.g., Korista & Goad 2004; Goad & Korista 2014; Lawther et al. 2018) to investigate how the emission line responsivity depends on factors, including the continuum state, driving continuum variability, BLR geometry, and the duration/cadence of the campaign. Korista & Goad (2004) calculated photoionization models suitable for NGC 5548, and found that the local line responsivity could be two times lower in the high continuum state than that in the low state (their Figure 3) with a factor of $\sim$8 times change in the continuum flux. In this case, the Hβ responsivities, estimated using the $F_{\rm var}$ ratio of the line to the continuum as suggested in Goad & Korista (2014), are $\sim$1.3 and 0.34 for the two years, respectively. But the continuum flux F_{5100} is only slightly higher (<5% on average, see Figure 4 panel (a)) in the second year. Note that the ionizing UV continuum may has larger variability between the two years than F_{5100}. Its amplitude and impact on the responsivity need to be confirmed by further observations and calculations. Goad & Korista (2014) show that continuum variations faster than the maximum time lag for an extended BLR reduce the measured line responsivity and also the time lag in the meantime (their Figure 9). The continuum variability timescale in the second year seems to be somewhat faster than that in the first year by comparing the widths of the two ACFs in Figure 5, but the measured Hβ time lag does not become shorter accordingly as expected if the variability timescale is the reason for the weaker response. Thus, factors other than the continuum flux state and variability timescale are needed to interpret the much weaker responsivity in the second year. Detailed calculations and simulations out of the scope of this paper are necessary to answer this question.

5.4. Comparing with Previous Campaigns

As mentioned previously, three campaigns have been done for PG 2130+099, including Kaspi et al. (2000) and Grier et al. (2008, 2012) before the present work. Since the Kaspi et al. (2000) campaign has poor sampling and the Grier et al. (2008) campaign is too short in duration, we only compare our results with Grier et al. (2012), which performed a cadence of roughly one day. Grier et al. (2012) obtained $\tau_{\rm H\beta} = 9.7 \pm 1.3$ days, which is shorter than the value measured in this campaign by a factor of larger than two. Considering that our campaign is 7 yr later than that of Grier et al. (2012), the difference could be real and due to changes of the BLR. However, Bentz et al. (2013) argued that the Grier et al. (2012) campaign missed some key observation dates and PG 2130+099 should have a lag of 31 ± 4 days from their reanalysis. This corrected time lag is in agreement with the present results.

6. Summary

We report a successive two-year campaign of PG 2130+099 using the CAHA 2.2 m and other telescopes since 2017. Reverberations of several broad emission lines are analyzed. We find the following:

1. From the observations in 2017, Hβ displayed a lag of $\tau_{\rm H\beta} = 22.6^{+2.7}_{-3.6}$ days. He I, He II, and Fe II have lags of $\tau_{\rm He\,I} = 18.2^{+7.3}_{-3.1}$ days, $\tau_{\rm He\,II} = -1.4^{+6.8}_{-0.9}$ days, and $\tau_{\rm Fe\,II} = 35.3^{+8.2}_{-9.9}$ days, respectively. The velocity-resolved delays of Hβ shows a sign of virialized motion. The BLRs are radially stratified (i.e., an onion structure) according to the full width at half maximum of the lines and the ionization energies of the ions.
2. From the observations in 2018, we obtain $\tau_{\rm H\beta} = 27.8^{+2.9}_{-2.9}$ days, $\tau_{\rm He\,I} = 31.1^{+2.9}_{-5.8}$ days, $\tau_{\rm He\,II} = -2.9^{+1.5}_{-0.9}$ days, and $\tau_{\rm Fe\,II} = 23.1^{+3.4}_{-5.6}$ days. The Hβ velocity-resolved delays favor an inflow as the variable part of the BLR. It is clear that the onion structure is broken in 2018 with a timescale less than one year.
3. We prefer the estimation of black hole mass from the first year observations. Using the black hole mass of $M_{\bullet} = 0.97^{+0.15}_{-0.18} \times 10^7\,M_{\odot}$, we estimate an accretion rate of $10^{2.1\pm0.5}\,L_{\rm Edd}/c^2$, suggesting that it is a super-Eddington accretor.
4. Our two-year high-cadence campaign shows several puzzles of the BLR reverberations in PG 2130+099. The stratified structure of Hβ, He I, and Fe II-emitting regions changes, and the kinematics of Hβ-emitting region changes from a virialized motion to an inflow, with a timescale less than one year. The mean spectra are less variable, but the line responsivity becomes much weaker in the second year. It is worth continuing intensive monitoring of PG 2130+099 to resolve these questions.

PG 2130+099 shows interesting reverberation behavior in our high-cadence campaign. MCMC simulations of the BLR (Pancoast et al. 2011; Li et al. 2018) will be carried out for detail explanations and better understandings.

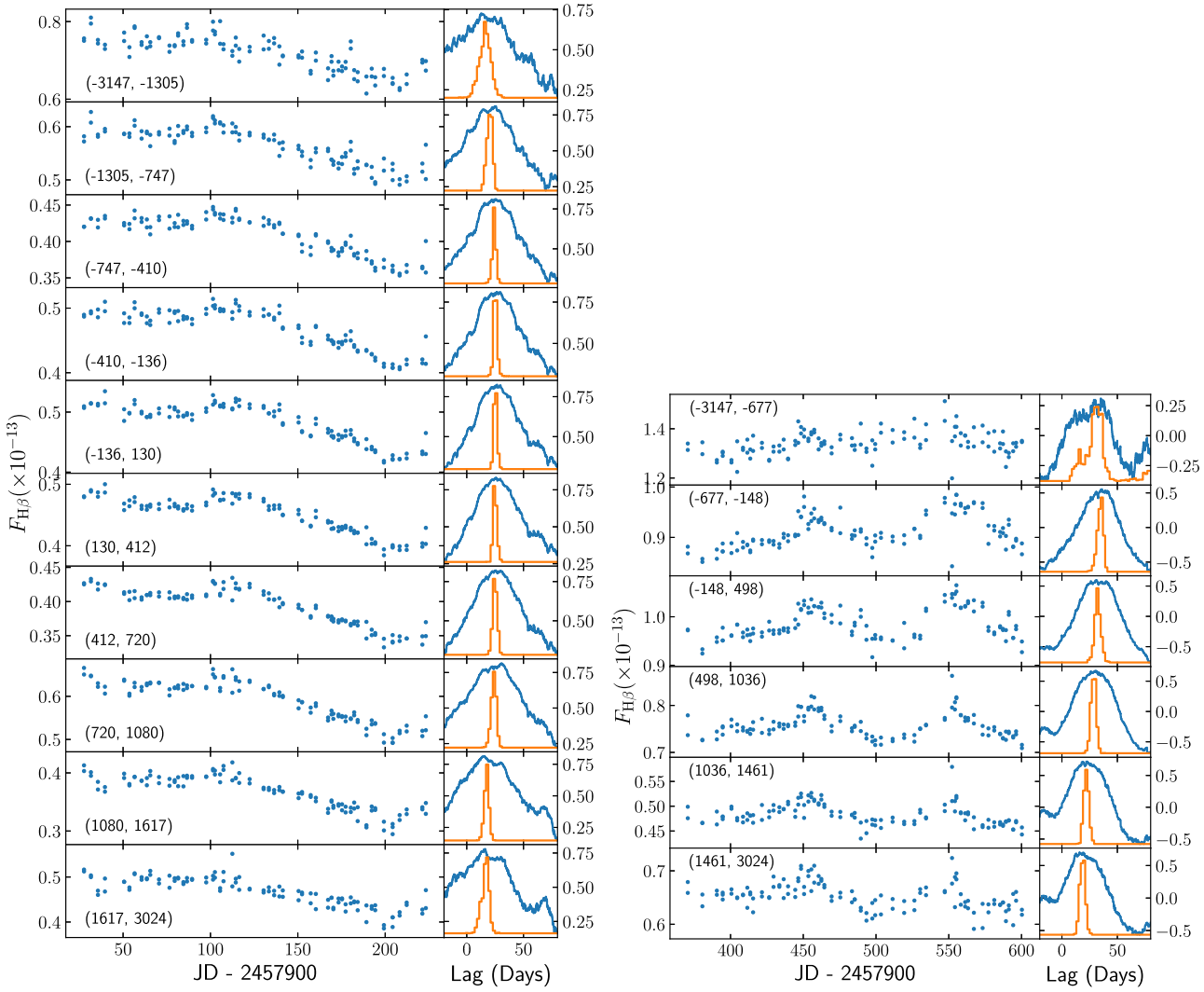

Figure 9. Hβ light curves and CCF analysis in each velocity bin with equal flux in the rms spectrum, from 2017 (left) and 2018 (right) observations. The blue curves are CCF functions and yellow lines are Monte Carlo simulations as described in the main text. The velocity boundaries are given by numbers in the brackets.

The authors are grateful to an anonymous referee for very useful reports. The campaign made use of mainly the CAHA 2.2 m, and jointly the Lijiang 2.4 m and the Sutherland 1.9 m telescopes, we acknowledge the support of the staff of these telescopes. This work is based on observations collected at the Centro Astronomico Hispanoen Andalucia (CAHA) at Calar Alto, operated jointly by the Andalusian Universities and the Instituto de Astrofisica de Andalucia (CSIC). Funding for the Lijiang 2.4m telescope has been provided by Chinese Academy of Sciences (CAS) and the People's Government of Yunnan Province. This research is supported by grant 2016YFA0400700 from the Ministry of Science and Technology of China, by NSFC grants NSFC-11773029, -11833008, -11991054, -11922304, -11873048, -11690024, and -11703077, by the CAS Key Research Program through KJZD-EW-M06, by the Key Research Program of Frontier Sciences, CAS, grant QYZDJ-SSW-SLH007.

Appendix A
CCF Analysis in Each Velocity Bin

Figure 9 shows Hβ light curves, CCFs, and CCCDs in each velocity bin with equal flux in the rms spectrum, used in Figure 6.

Appendix B
Velocity-resolved Delays with Equal Fluxes in the Mean Spectra

Considering that the rms spectrum could be contaminated by continuum, we calculated the Hβ velocity-resolved delays in each velocity bin with equal flux in the mean spectrum, shown

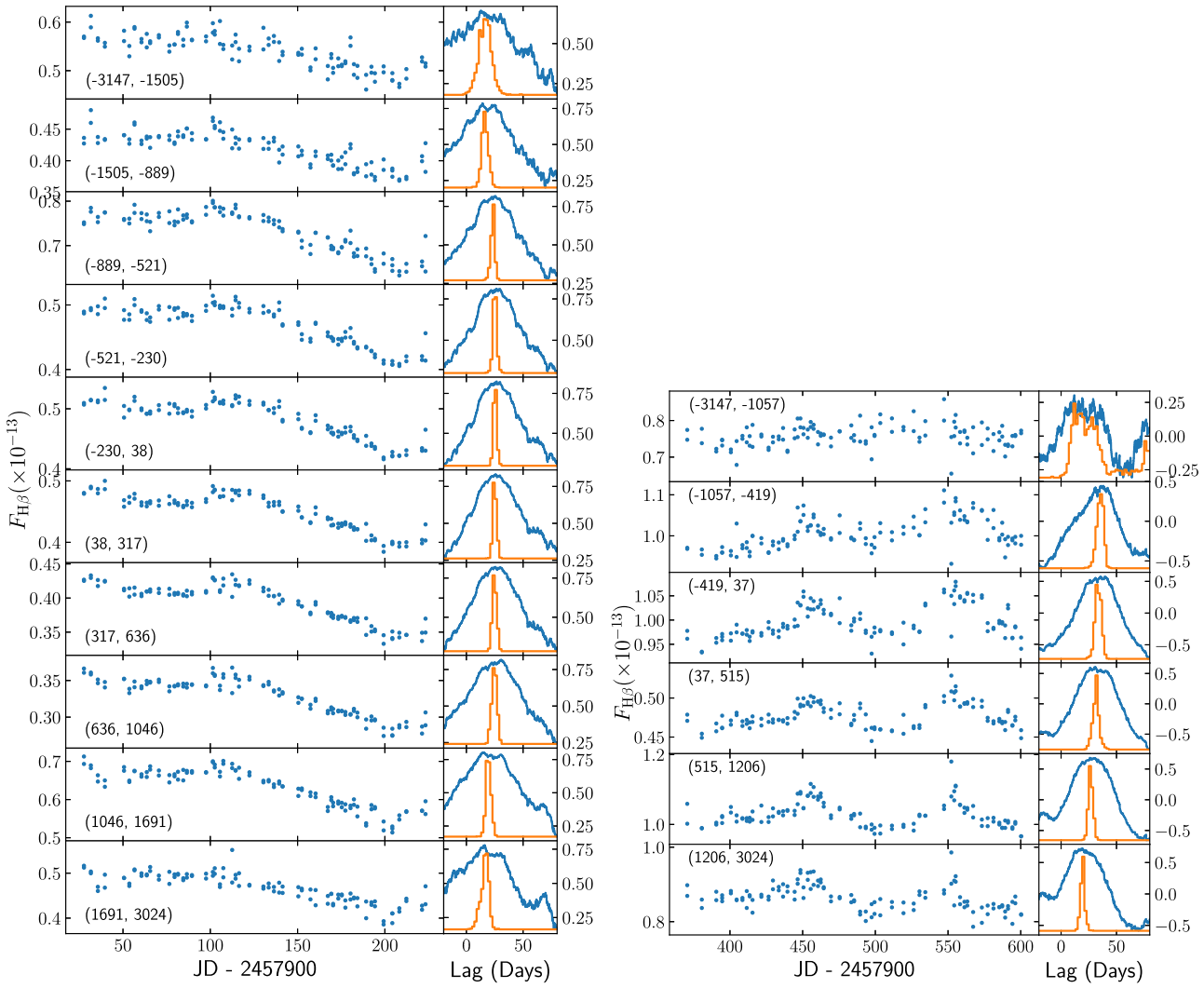

Figure 10. Hβ light curves and CCF analysis in each velocity bin with equal flux in the mean spectrum, from 2017 (left) and 2018 (right) observations. The blue curves are CCF functions and yellow lines are Monte Carlo simulations. The velocity boundaries are given in the brackets.

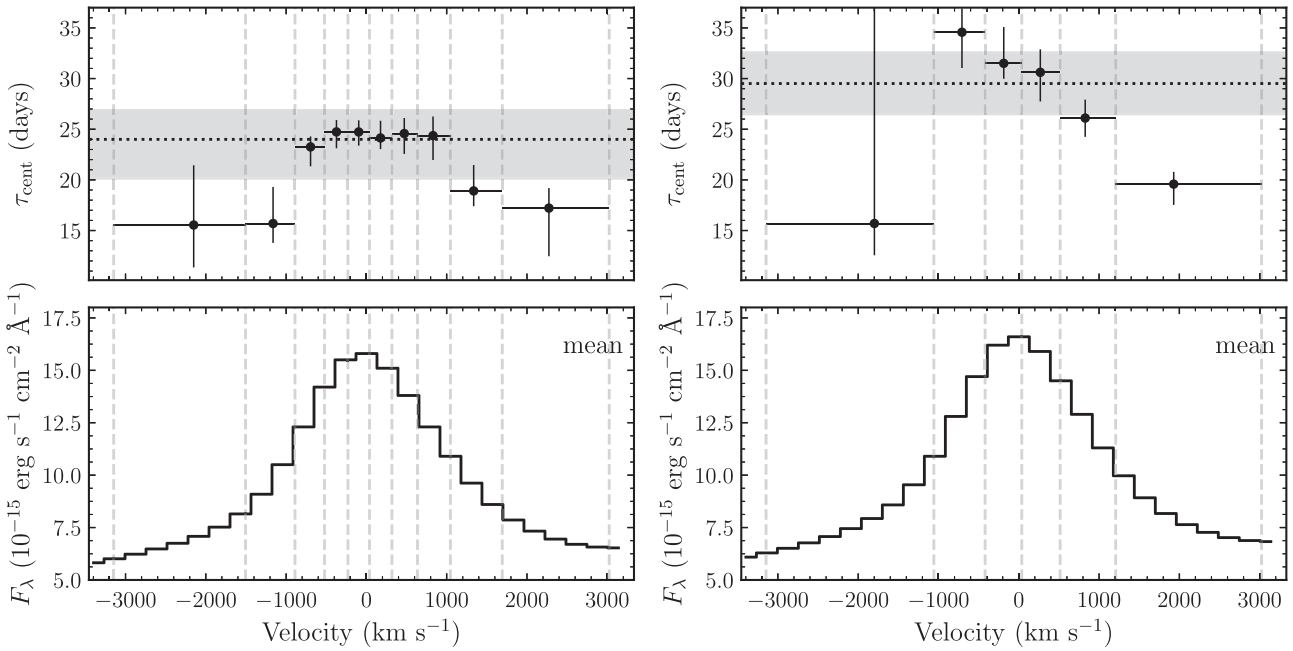

Figure 11. Velocity-resolved delays in each velocity bin with equal flux in the mean spectrum, for 2017 (left) and 2018 (right) observations.

in Figure 11. Light curves in each velocity bin are given in Figure 10. Comparing Figure 6 with 11, we find that the two kinds of velocity-resolved delays are quite similar. Therefore the influence of continuum contamination is not important.

ORCID iDs

Yan-Rong Li https://orcid.org/0000-0001-5841-9179
Pu Du https://orcid.org/0000-0002-5830-3544
Kai-Xing Lu https://orcid.org/0000-0002-2310-0982
Luis C. Ho https://orcid.org/0000-0001-6947-5846
Wei-Hao Bian https://orcid.org/0000-0002-2121-8960
Michael S. Brotherton https://orcid.org/0000-0002-1207-0909
Hartmut Winkler https://orcid.org/0000-0003-2662-0526
Jian-Min Wang https://orcid.org/0000-0001-7617-4232

References

Bachall, J. N., Kozlovsky, B. N., & Salpeter, E. E. 1972, ApJ, 171, 467
Barth, A. J., Bennert, V. N., Canalizo, G., et al. 2015, ApJS, 217, 26
Barth, A. J., Pancoast, A., Bennert, V. N., et al. 2013, ApJ, 769, 128
Batiste, M., Bentz, M. C., Raimundo, S. I., et al. 2017, ApJL, 838, L10
Bentz, M., Peterson, B. M., Netzer, H., Pogge, R. W., & Vestergaard, M. 2009, ApJ, 697, 160
Bentz, M. C., Denney, K. D., Grier, C. J., et al. 2013, ApJ, 767, 149
Bian, W.-H., Huang, K., Hu, C., et al. 2010, ApJ, 718, 460
Blandford, R. D., & McKee, C. F. 1982, ApJ, 255, 419
Boroson, T. A., & Green, R. F. 1992, ApJS, 80, 109
Bruzual, G., & Charlot, S. 2003, MNRAS, 344, 1000
Cardelli, J. A., Clayton, G. C., & Mathis, J. S. 1989, ApJ, 345, 245
Collin-Souffrin, S., & Lasota, J.-P. 1988, PASP, 100, 1041
Du, P., Hu, C., Lu, K.-X., et al. 2014, ApJ, 782, 45
Du, P., Hu, C., Lu, K.-X., et al. 2015, ApJ, 806, 22
Du, P., Lu, K.-X, Hu, C., et al. 2016a, ApJ, 820, 27
Du, P., Lu, K.-X., Zhang, Z.-X., et al. 2016b, ApJ, 825, 126
Du, P., Zhang, Z.-X., Wang, K., et al. 2018, ApJ, 856, 6
Edelson, R., Gelbord, J., Cackett, E., et al. 2019, ApJ, 870, 123
Edelson, R., Turner, T. J., Pounds, K., et al. 2002, ApJ, 568, 610
Fausnaugh, M. M. 2017, PASP, 129, 4007
Gaskell, C. M., & Peterson, B. M. 1987, ApJS, 65, 1
Gaskell, C. M., & Sparke, L. S. 1986, ApJ, 305, 175
Goad, M. R., & Korista, K. T. 2014, MNRAS, 444, 43
Grier, C. J., Martini, P., Watson, L. C., et al. 2013a, ApJ, 773, 90
Grier, C. J., Peterson, B. M., Bentz, M. C., et al. 2008, ApJ, 688, 837
Grier, C. J., Peterson, B. M., Horne, K., et al. 2013b, ApJ, 764, 47
Grier, C. J., Peterson, B. M., Pogge, R. W., et al. 2012, ApJ, 755, 60
Grier, C. J., Trump, J. R., Shen, Y., et al. 2017, ApJ, 851, 21
Ho, L. C., & Kim, M. 2014, ApJ, 789, 17
Ho, L. C., & Kim, M. 2015, ApJ, 809, 123
Horne, K., Peterson, B. M., Collier, S. J., & Netzer, H. 2004, PASP, 116, 465
Hu, C., Du, P., Lu, K.-X., et al. 2015, ApJ, 804, 138
Hu, C., Wang, J.-M., Ho, L. C., et al. 2016, ApJ, 832, 197
Kaspi, S., Smith, P. S., Netzer, H., et al. 2000, ApJ, 533, 631
Kim, M., Ho, L. C., Peng, C. Y., Barth, A., & Im, M. 2017, ApJS, 232, 21
Koratkar, A. P., & Gaskell, C. M. 1991, ApJS, 75, 719
Korista, K. T., & Goad, M. R. 2004, ApJ, 606, 749
Kormendy, J., & Ho, L. C. 2013, ARA&A, 51, 511
Lawther, D., Goad, M. R., Korista, K. T., et al. 2018, MNRAS, 481, 533
Li, Y.-R., Songsheng, Y.-Y., Qiu, J., et al. 2018, ApJ, 869, 137
Li, Y.-R., Wang, J.-M., & Bai, J.-M. 2016, ApJ, 831, 206
Lü, X.-R. 2008, ChJA&A, 8, 50
Maoz, D., & Netzer, H. 1989, MNRAS, 236, 21
Mejía-Restrepo, J. E., Lira, P., Netzer, H., Trakhtenbrot, B., & Capellupo, D. M. 2017, NatAs, 2, 63
O'Donnell, J. E. 1994, ApJ, 422, 158
Onken, C. A., Ferrarese, L., Merritt, D., et al. 2004, ApJ, 615, 645
Pancoast, A., Brewer, B. J., & Treu, T. 2011, ApJ, 730, 139
Peterson, B. M. 2014, SSRv, 183, 253
Peterson, B. M., Denney, K. D., De Rosa, G., et al. 2013, ApJ, 779, 109
Peterson, B. M., Ferrarese, L., Gilbert, K. M., et al. 2004, ApJ, 613, 682
Peterson, B. M., & Wandel, A. 1999, ApJL, 521, L95
Peterson, B. M., Wanders, I., Bertram, R., et al. 1998a, ApJ, 501, 82
Peterson, B. M., Wanders, I., Horne, K., et al. 1998b, PASP, 110, 660
Rodríguez-Pascual, P. M., Alloin, D., Clavel, J., et al. 1997, ApJS, 110, 9
Rybicki, G. B., & Press, W. H. 1992, ApJ, 398, 169
Schlafly, E. F., & Finkbeiner, D. P. 2011, ApJ, 737, 103
Shakura, N. I., & Sunyaev, R. A. 1973, A&A, 24, 337
Veilleux, S., & Osterbrock, D. E. 1987, ApJS, 63, 295
Welsh, W. F., & Horne, K. 1991, ApJ, 379, 586
White, R. J., & Peterson, B. M. 1994, PASP, 106, 879
Whittle, M. 1992, ApJS, 79, 49
Winkler, H., & Paul, B. 2017, arXiv:1708.02056
Woo, J.-H., Yoon, Y., Park, S., et al. 2015, ApJ, 801, 38
York, D. G., Adelman, J., Anderson, J. E., et al. 2000, AJ, 120, 1579